Size-dependent geometrically necessary dislocation structures in single-crystalline tungsten

Jin Wang[1,2,a] , Likang Luan[2], Tillmann Volz[3,4], Sabine M. Weygand[4], Ruth Schwaiger[1,2,5,a]

[1] Institute of Energy and Climate Research, Forschungszentrum Juelich GmbH, 52425 Juelich, Germany
[2] Institute for Applied Materials, Karlsruhe Institute of Technology (KIT), 76344 Eggenstein-Leopoldshafen, Germany
[3] Center of Applied Research, Karlsruhe University of Applied Sciences, 76012 Karlsruhe, Germany
[4] Faculty of Mechanical Engineering and Mechatronics, Karlsruhe University of Applied Sciences, 76012 Karlsruhe, Germany
[5] Chair of Energy Engineering Materials, Faculty 5, RWTH Aachen University, 52056 Aachen, Germany
[a] Address all correspondence to these authors. e-mails: jin.wang@fz-juelich.de; r.schwaiger@fz-juelich.de

Wedge indentation experiments were conducted to study the depth dependence of geometrically necessary dislocation (GND) structures in single-crystalline tungsten. Single-crystalline tungsten exhibits a pronounced indentation size effect (ISE), which can be rationalized based on GNDs. The dislocation mechanisms, however, are still under debate. Due to the plane strain condition during the wedge indentation, the dislocations in the cross sections underneath indents could be analyzed based on the Nye tensor and the lattice rotations determined using transmission Kikuchi diffraction. The dislocation structures depend on the size of the indent confirming the different hardness regimes and the bilinear ISE reported recently. For shallow indents, the dislocations are rather localized at the tip of the indent, while with increasing depth the dislocation volume expands; subgrains and distinct rays of increased dislocation density form. At larger depths, the indentation-induced deformation fields exhibit characteristics similar to the kink-type shear at a stationary crack tip.

Introduction

Tungsten and tungsten alloys have outstanding mechanical and physical properties at high temperatures [1, 2] and therefore great potential as structural materials in high-temperature energy conversion systems. The brittle-to-ductile transition occurs at rather high temperatures, though, which limits the usage of tungsten and tungsten alloys as structural materials. Therefore, a comprehensive understanding of dislocation glide and of the mechanisms controlling the deformation of tungsten is needed.

In many single crystalline metals with body-centered cubic (bcc) and face-centered cubic (fcc) crystal structures, a size effect of the mechanical properties has been observed [3], while the properties of macroscale samples are independent of the specimen size. In indentation testing, this phenomenon is reflected as an increase of the hardness with decreasing indentation depth, which is known as the indentation size effect (ISE). By contrast, for large indents made with pyramidal or conical indenters, the hardness values remain constant. The size dependence of indentation hardness has been observed for a range of different

materials and associated with strain gradients related to geometrically necessary dislocations (GNDs) underneath an indent (e.g., [4]). The overall trend observed in experiments is comparable, but different characteristics of the ISE in particular in the low depth regime have been observed. The data presented in a number of studies [5–8] point toward different depth regimes for the ISE of tungsten . The Nix-Gao model [9], which is well accepted as a description of the ISE, fails to describe the hardness increase in tungsten for depths less than ~ 300 nm [8].

Recently, a modification of the original Nix-Gao model was suggested to capture the full depth regime, which is based on an evolving GND volume that is significantly affected by the surrounding elastically deformed material until full contact is achieved [8]. Such a dynamical picture predicts clear differences in the dislocation microstructures for different indentation depths, though, which have not been studied in greater detail yet. Only few studies of dislocation microstructures related to the ISE of tungsten have been reported [7, 10]. In those studies, variations of the misorientation [10] and GND distributions [7] with size of the indents were reported. A gradual decrease of

GND density from the indent center to the edge was observed for shallow depth indents, while the GNDs appeared more evenly distributed [7].

GND densities can be estimated from the measurements of the lattice misorientation using electron backscatter diffraction (EBSD) [11] based on the fundamental equations of continuum dislocation theory established by Nye [12] and Kroener [13]. Two-dimensional EBSD studies, which are typically conducted, have the limitation that out-of-plane lattice rotation is generally not accessible. Combining EBSD with serial sectioning using a Focused Ion Beam (FIB) allows mapping the three-dimensional lattice rotation fields [14–16]. Alternatively, a two-dimensional deformation condition can be introduced deliberately to ensure that all out-of-plane components are zero, as employed to study cracks [17] and wedge indentation of fcc single crystals [18–20].

In this study, we investigated the size and strain rate dependencies of the GNDs underneath indents into tungsten single crystals with a (001) out-of-plane orientation. In our previous work, we have shown that different regimes of the size-dependent hardness of tungsten exist [8], which are likely related to the evolution of the GND structure during plastic deformation. To resolve the dislocation structures down to indentation depths < 300 nm, we employed the transmission Kikuchi diffraction (TKD) method, which was shown to resolve the local crystal orientations in a range < 20 nm [21–24]. The tungsten single crystals were indented under plane strain conditions using a wedge-shaped indenter tip. Based on the crystal lattice rotation determined by TKD, we calculated the GND density according to the Nye-Kröner tensor [12, 13] and analyzed the dislocation structures for different indentation depths and strain rates.

Results

Orientation maps determined by TKD

The crystallographic orientation of the cross section at mid-length of the wedge indent is shown as inverse pole figure (IPF) map in Fig. 1 for the three orthogonal directions. The rolling direction (RD) in Fig. 1(a), transverse direction (TD) in Fig. 1(b), and normal direction (ND) in Fig. 1(c) are equivalent to the x_1, x_2, x_3 directions defined in Fig. 3(a) later. Before deformation, the original crystallographic orientation was confirmed as indicated in Fig. 1(a).

The change of color in Fig. 1(a) and (b) indicates that after wedge indentation, the crystal orientation changes in the deformed region underneath the indent. In the rolling and transverse directions, in-plane rotation can be seen. As indicated by the IPF triangle (Fig. 1), the lattice tends to rotate toward a ⟨111⟩ orientation from the initial orientation, which was ⟨011⟩ in RD and ⟨001⟩ in TD. Underneath the tip of the indent along the center line, no change of the crystal orientation can be seen. In the normal direction [Fig. 1(c)], no lattice rotation was observed. Near the indented surface, subgrains and low-angle grain boundaries have formed on both sides underneath the faces of the indent. With increasing distance from the surface, the deformation becomes less pronounced. Furthermore, the orientation of the subgrains is not yet homogeneous, and the orientation gradient indicates that the stress-induced crystallization has not yet been completed. These features were observed in all lamellae prepared from wedge indents under different loading conditions.

The quantitative characterization of the plane strain deformation revealed in Fig. 1 is achieved by comparing the value of the Euler angles of the deformed area to the Euler angles of the undeformed area. The reference Euler angles (φ_1, Φ, φ_2) of the undeformed material were determined over an area far away from the indent. Based on these reference angles and comparing them to the orientation of the individual measurement points, the difference ($d\varphi_1$, $d\Phi$, $d\varphi_2$) describes the lattice rotation angles. The lattice rotation can be split into in-plane rotation ($d\varphi_1$ and $d\varphi_2$) and out-of-plane rotation $d\Phi$. The results shown in Fig. 1 are presented as lattice rotation maps in Fig. 2.

In-plane lattice rotations occur anti-symmetrically with rotation angles reaching ± 20° (Fig. 2). An almost zero out-of-plane rotation is observed confirming the plane strain assumption. The maximum angles in the in-plane map are found close to the deformed surface in the regions containing the subgrains.
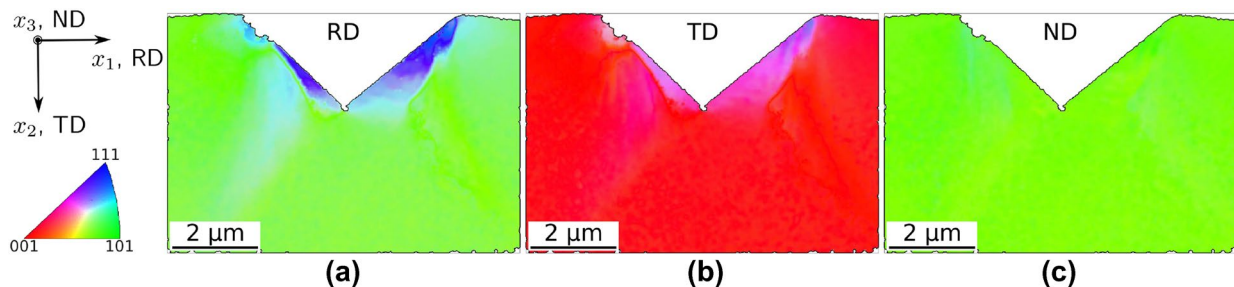

Figure 1: IPF map of three orthogonal directions (a) RD, (b) TD, and (c) ND in a cross section through a wedge indent to 2000 nm at a strain rate of 0.05 s^{-1}. The TKD measurement was conducted with the e^{-1}Flash^{HD} and a step size of 17 nm.
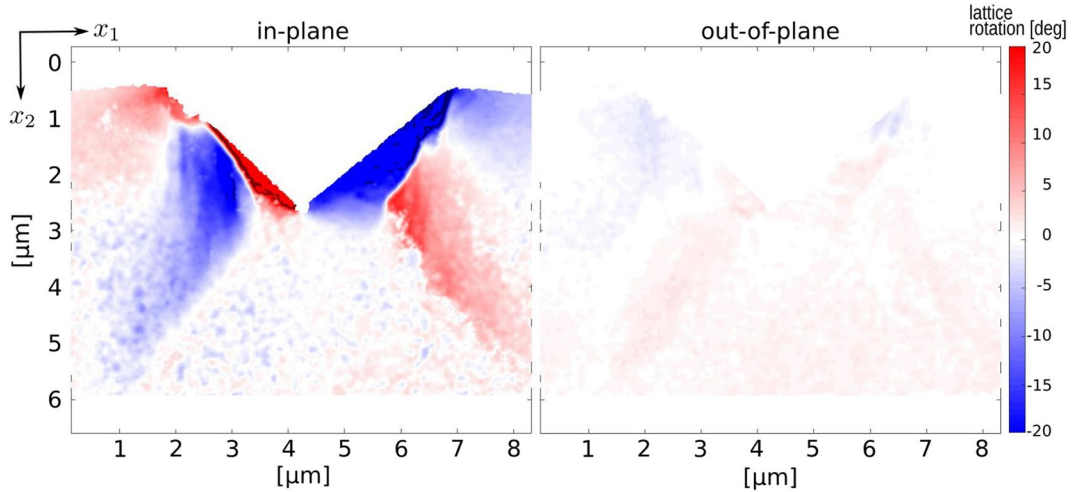
Figure 2: Calculated lattice rotation maps showing the in-plane rotation (left-hand side) and out-of-plane rotation (right-hand side). The out-of-plane rotation is almost zero confirming the plane strain deformation. The slight deviation from zero for the out-of-plane case is related to uncertainties during sample mounting.
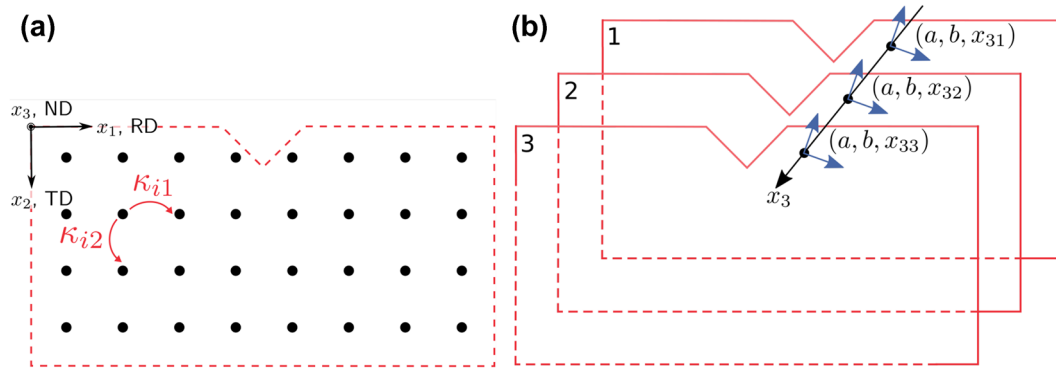

Figure 3: (a) Schematic of the determination of the curvature κ_{ij} using the TKD data of the cross section of an indent [25]. Black dots represent the TKD measurement points with their coordinates (x_1, x_2) and orientations recorded. Here, x_1 and x_2 are the rolling direction (RD) and transverse direction (TD), respectively. x_3 is the normal direction (ND). (b) Schematic representation of points in the same position $(x_1, x_2)=(a, b)$ at different positions (1, 2, 3...) along the x_3 axis. Under plane strain conditions, the misorientation between these points is equal to zero.

Pronounced discontinuities can be seen at the subgrain boundaries as well as at the transitions between the different sectors. In the region underneath the apex of the indent between the blue and red sectors on the left- and right-hand side, respectively, the lattice rotation is almost zero.

Data analysis

The dislocation density ρ can be determined using the dislocation tensor α_{ij} [13]:

$$\alpha_{ij} = \rho b_i \otimes t_j \tag{1}$$

with b_i and t_j as the components of the Burgers vector **b** and the line tangent vector **t** of the GNDs, respectively, with indices $i, j \in \{1, 2, 3\}$. The α_{ij}, also known as the Nye tensor, can be approximated by the curvature κ [12, 25]:

$$\kappa_{ij} = \frac{\partial \theta_i}{\partial x_j}, \tag{2}$$

where $\partial \theta_i$ is the change of orientation angle, namely the lattice rotation about the axis x_i, and ∂x_j the displacement vector along axis x_j [12, 19]. In the experiment, as the ∂x_j is equal to the step size dx_j, ∂x_j can be written as dθ_i. Figure 3(a) shows a schematic of an indented sample coordinate system, with the TKD measurement points and the curvature tensor κ_{ij}.

According to Nye [12], the three-dimensional dislocation tensor α_{ij} can be replaced by curvature vectors yielding the Nye tensor:

$$\alpha_{ij} = \begin{pmatrix} -(\kappa_{22} + \kappa_{33}) & \kappa_{21} & \kappa_{31} \\ \kappa_{12} & -(\kappa_{11} + \kappa_{33}) & \kappa_{32} \\ \kappa_{13} & \kappa_{23} & -(\kappa_{11} + \kappa_{22}) \end{pmatrix}. \tag{3}$$

Combining Eqs. 1 and 3, the dislocation density ρ can be experimentally determined.

Note that in Eq. 3, components including κ_{i3} would require experimental data from the out-of-plane deformation, i.e., along x_3 [Fig. 3(a)]. If plane strain deformation is achieved on the measurement surface [19, 20, 26], the 3D case is reduced to two dimensions. For both bcc and fcc materials, according to Rice [26], the plane strain is associated with tensile cracks with crack plane and growth direction (010) and [101], respectively, or crack plane (101) and direction [010]. This prediction has indeed been observed confirming the plane strain deformation [17, 27]. Equivalent loading condition can be realized by indentation experiments if a line load along one of the defined directions instead of a point load is applied [19, 20].

Thus, if the lattice rotation occurs only around the x_3-axis, $d\theta_3$ is the only non-zero rotation. The components κ_{1j} and κ_{2j} in Eq. 3 are equal to zero, since $d\theta_1$ and $d\theta_2$ are zero (Eq. 2). Furthermore, for plane strain conditions, points having the same coordinates (x_1, x_2) but different x_3 [see Fig. 3(b)] will have identical crystallographic orientations along the x_3 axis after deformation, since only in-plane rotation in the (x_1, x_2) plane occurs.

Figure 3(b) illustrates why the component κ_{33} is equal to zero for plane strain deformation. The Kröner-Nye tensor (Eqs. (2) and (3)) can thus be simplified:

$$\begin{pmatrix} 0 & 0 & \kappa_{31} \\ 0 & 0 & \kappa_{32} \\ 0 & 0 & 0 \end{pmatrix} = \rho b_i \otimes t_j, \qquad (4)$$

with $i, j \in \{1, 2, 3\}$. The slip systems were defined by assigning the corresponding Burgers vector **b** and line tangent vector **t**. For single-crystalline tungsten, the following glide systems were analyzed: $\{110\}\langle111\rangle$, $\{112\}\langle111\rangle$, $\{123\}\langle111\rangle$. The line tangent vector for edge dislocations t_e is determined by the Burgers vector **b** and the normal vector of the slip plane **n** as $t_e = \mathbf{b} \times \mathbf{n}$, and for screw dislocations $t_s = \mathbf{b}$ along the $\langle111\rangle$ directions [25]. Therefore, the GND density ρ can be resolved for the individual slip systems. The total GND density ρ_{total} is easily calculated:

$$\rho_{total} = \sum_n \rho_n. \qquad (5)$$

Here, n stands for the number of independent slip systems.

Since a few points may not be indexed in the TKD measurements, the experimental data were smoothed by a spline fit to avoid artifacts in the subsequent calculation steps (see Supplementary materials).

The GND density was analyzed based on the TKD data using Eqs. (4) and (5). Figure 4 shows the GND density distributions at 2000 nm depth for the different slip systems, i.e., $\{110\}\langle111\rangle$ edge dislocations, $\{112\}\langle111\rangle$ edge dislocations, $\{123\}\langle111\rangle$ edge dislocations, and $\langle111\rangle$ screw dislocations. The data analyzed is the same as shown in Figs. 1 and 2.

At 2000 nm depth and 0.05 s^{-1} indentation strain rate, the $\{110\}\langle111\rangle$ system [Fig. 4(a)] is the only activated slip system of edge dislocations. The background noise visible in Fig. 4(b)–(d) is related to the FIB preparation process and homogeneous over the cross section. No screw dislocations were observed [Fig. 4(d)], as expected due to the plane strain condition. Note, that the three components along the main diagonal in Eq. (4), i.e., the screw dislocation components [15], are equal to zero.

The total GND density (Fig. 5) was determined according to Eq. (5). The TKD data of cross sections at four different indentation depths and an indentation strain rate of 0.05 s^{-1} were analyzed. With increasing depth, more GNDs appear to be generated in order to adapt to the increasing deformation volume. The GND distributions exhibit different characteristics at different indentation depths, i.e., up to 200 nm, and in the range of 500 nm to 2000 nm, respectively. For the shallow indents [Fig. 5(a) and (b)], the GNDs appear to be localized around the indents with the highest GND density close to the surface. No significant differences of the GND structures can be seen at 150 nm and 200 nm. However, for the deep indents, i.e., at 500 nm and 2000 nm depth, the dislocation structures are distinctly different from those underneath the shallow indents. For 500 nm depth, a dense line of GNDs reaches from the surface into the bulk, and subgrains have formed [blue arrow in Fig. 5(c)]. Furthermore, for both 500 nm and 2000 nm depth, two symmetric lines of higher GND density were observed beneath the subgrains at angles of ~ 35° to the vertical axis [black arrows in Fig. 5(c) and (d)]. In the lattice rotation maps (Fig. 2), the boundaries of the lattice rotation sectors correspond to these lines of increased GND density. At the maximum depth of 2000 nm, no further changes were observed, and the general characteristics of the GND structures observed at 500 nm depth remain stable. In addition to the depth dependence, the GND structures were affected by the indentation strain rate. Figure 6 shows the comparison of the GND distributions at two strain rates, i.e., 0.005 s^{-1} and 0.5 s^{-1}, in the two depth regimes.

Similar behavior can be seen in the cross sections showing the GND densities in Fig. 6. Comparing the samples in the same depth regimes at different strain rates, more GNDs appear to be generated at the higher strain rates. This behavior is correlated to the higher hardness values at higher strain rates [8]. Comparing the slow and fast indents at 2000 nm depth [Fig. 6(c) and (d)], subtle differences in the subgrain regions can be seen [marked by black arrows in Fig. 6(d)], while the general characteristics of the GND structures appear identical. The difference of the GND structures between the slow and fast indents is more significant in the small depth regime. While the slow, shallow indent in Fig. 6(a) hardly shows the concentrated GND features, the GND
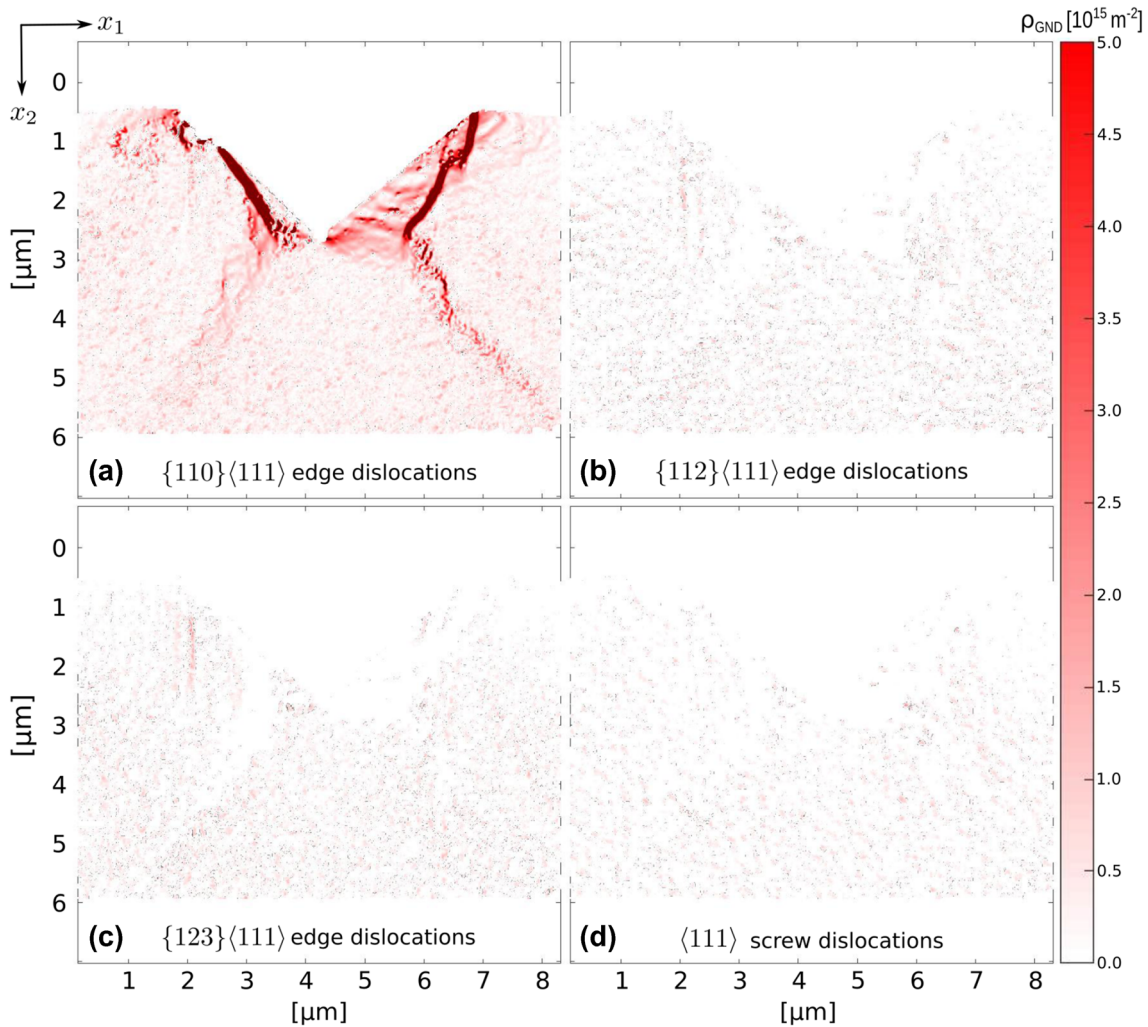
Figure 4: GND density distributions of the different slip systems: (a) $\{110\}\langle111\rangle$ edge dislocations, (b) $\{112\}\langle111\rangle$ edge dislocations, (c) $\{123\}\langle111\rangle$ edge dislocations, (d) $\langle111\rangle$ screw dislocations. The indentation experiment was conducted at an indentation strain rate of 0.05 s^{-1}. The step size of TKD measurement (e^{-1}Flash^{HD}) was 17 nm.

density in the fast indent [Fig. 6(b)] is apparently high enough to allow the formation of low-angle grain boundaries, as indicated by the black arrows.

Discussion

As shown above, we observed clear differences of the GND structures underneath the indents for different indentation depths and strain rates (Figs. 5 and 6), which we will discuss in this section. The difference of the GND densities at two different depths and strain rates is quantitatively shown as the mean GND density along the x_1 axis (Fig. 7). The GND densities at the different x_1 positions [RD in Fig. 3(a)] were averaged over a defined distance along the x_2 (TD) axis. Details regarding the averaging procedure can be found in the Supplementary materials.

In Fig. 7(a), the effect of misalignment between the normal loading axis of the indenter tip and the sample surface is clearly visible when the indentation depth is small, while the misalignment effect is less pronounced with the depth increasing. The mean GND density was quite asymmetric comparing the regions to the left and right of the shallow indents, while the asymmetry is less notable when the indentation depth increased [Fig. 7(b)]. In the center of the indent, i.e., at x_1=0, the GND density at both depths reaches a minimum. For the shallow indents, the difference between the mean GND densities at the two strain rates is greater than the difference at the larger depth. At the depth of 2000 nm, a slightly higher GND density was observed for the higher strain rate in the center region [the gray-shaded area in Fig. 7(b)], but overall both GND distributions are comparable. For the shallow indents, though, the strain rate has a more pronounced influence on the dislocation structures. While in terms
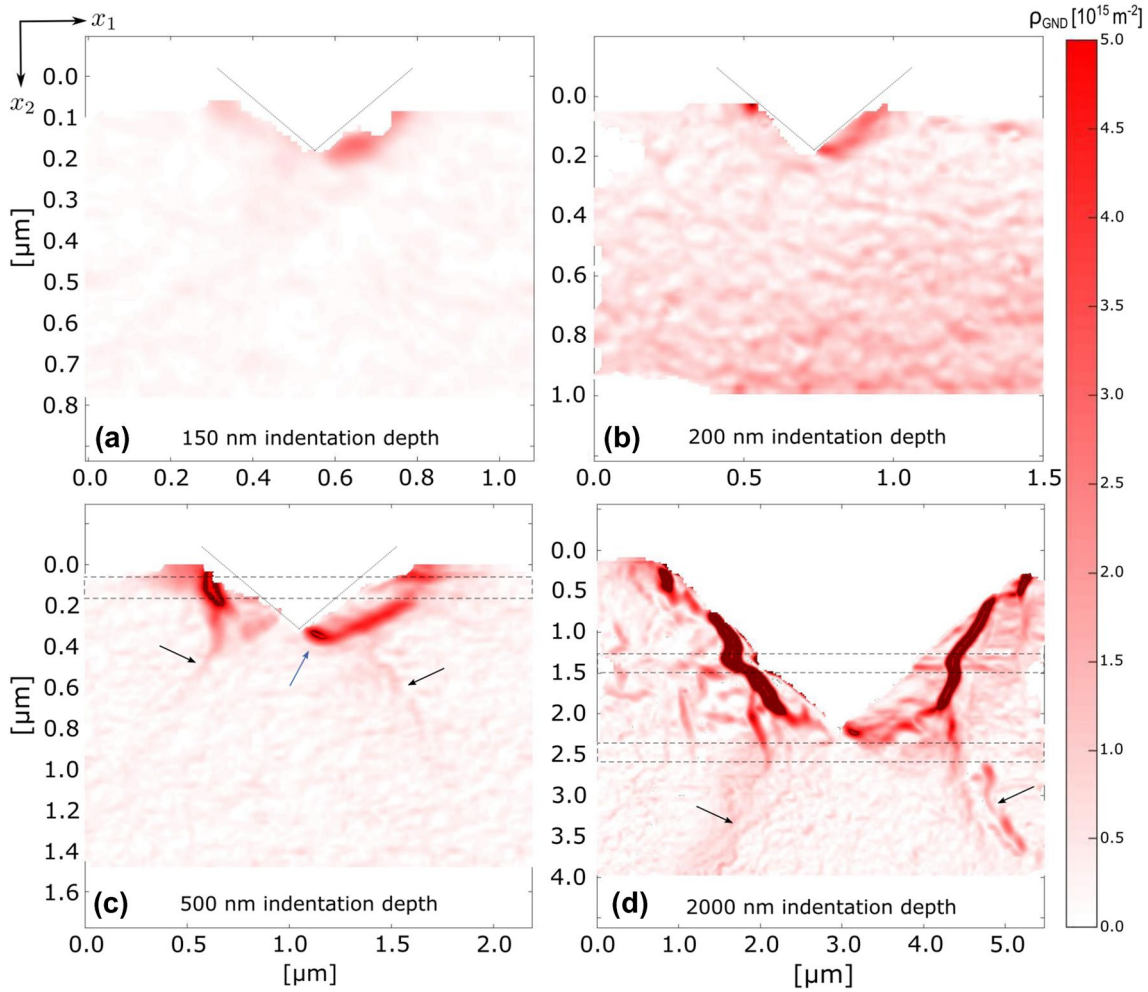
Figure 5: Total GND density distributions in the cross sections of wedge indents at strain rate of 0.05 s^{-1}, and different indentation depths of nominally (a) 150 nm, (b) 200 nm, (c) 500 nm, (d) 2000 nm. For small indents, the indent surface was marked by the gray dotted line. Notable features with higher dislocation densities are marked by blue and black arrows. The step size of the TKD measurements for (a) and (b) was 12 nm, for (c) 15 nm and (d) 20 nm. The TKD measurements were conducted with the AZtec EBSD system. Beam drift during scanning due to the scan time >2h caused horizontal shift of the data as marked by the black frames, which does not affect our general analysis.

of $1/h$, the difference between 150 and 200 nm is the same as the difference between 500 and 2000 nm, the difference of the GND densities in the low depth regime is smaller than the difference in the large-depth regime. Presuming the hardness is affected by the GND density, the difference between hardness values should, thus, be greater for shallow indents when comparing the data at different strain rates. Such behavior was indeed observed recently in indentation of tungsten using a Berkovich tip [8].

The order of magnitude of the total GND density of $\sim 10^{15}$ m^{-2} determined by our analysis is in the same range as the dislocation densities estimated based on the hardness data from Berkovich indentation to comparable depths [8] and the Nix–Gao model [9]. The hardness H of a material can be expressed as [9, 28]

$$H = 3\sqrt{3}\alpha\mu b\sqrt{\rho_S + \rho_G}, \qquad (6)$$

with $\alpha = 0.5$ as a constant characteristic of the dislocation structure [9], $\mu = 151.9$ GPa as the shear modulus, and b = 0.27353 nm as the magnitude of the Burgers vector of tungsten. ρ_S and ρ_G are the densities of the statistically stored dislocations and the GNDs, respectively. The dislocation densities ρ_S and ρ_G are then estimated according to

$$\rho_S = H_0^2\left(3\sqrt{3}\alpha\mu b\right)^{-2} \qquad (7)$$

and

$$\rho_G = \left(H^2 - H_0^2\right)\left(3\sqrt{3}\alpha\mu b\right)^{-2} \qquad (8)$$

with H_0 as the depth-independent hardness [9]. Assuming $H_0 = 4.2$ GPa for a {(001)} tungsten single crystal [5, 6, 8], $\rho_S \approx 1.5 \times 10^{15}$m^{-2}. Estimating a value of 6 GPa for H at a depth
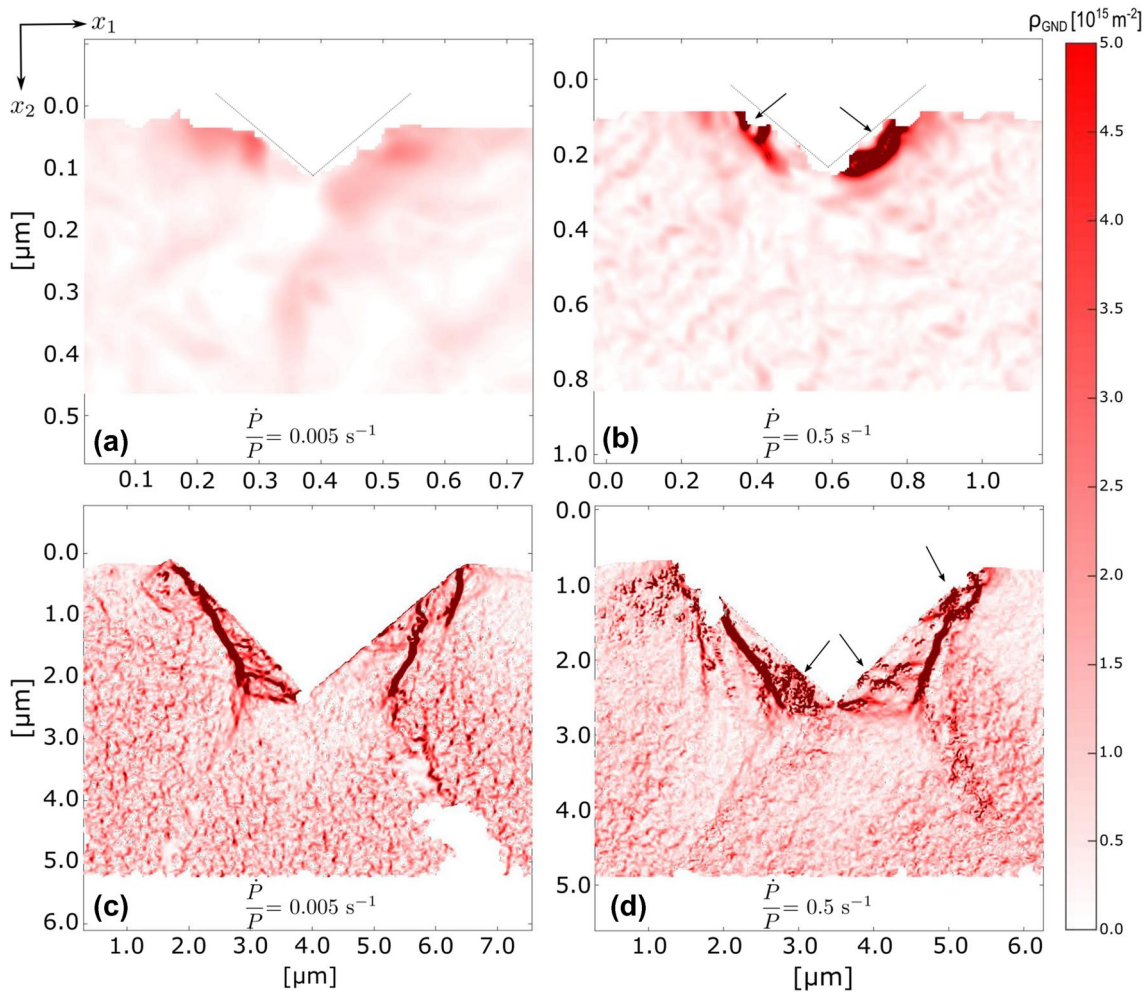
Figure 6: Total GND density distributions in the cross sections through wedge indents at two strain rates in the small and large depth regimes: (a) 0.005 s^{-1}, 200 nm; (b) 0.5 s^{-1}, 200 nm; (c) 0.005 s^{-1}, 2000 nm; and (d) 0.5 s^{-1}, 2000 nm. For small indents, the indent surface was marked by the gray dotted line. Clear differences between the two strain rates were observed (marked by the black arrows). The step size of the TKD measurement (e^{-1}Flash^{HD}) for the shallow indents and deep indents was 7 nm and 12 nm, respectively.

of ~500 nm [8], the average GND density in the hemi-spherical volume [9] $\rho_G \approx 1.5 \times 10^{15}$m^{-2}. While a direct comparison of this estimate to the dislocation densities determined over the cross sections underneath wedge indents cannot be made, the order of magnitude is comparable and supports the range of densities presented above.

The GND structures underneath the wedge indents into tungsten to different depths indicate that different deformation regimes exist, as also suggested in our recent study of the ISE [8]. While the ISE for depths greater than ~ 300 nm could be well described by the Nix-Gao model, as also observed in the literature [4, 5, 9, 29], the assumptions in the model had to be modified to capture the deformation at smaller depths. Based on our TKD results, we suggest the following changes to occur in the deformed volume underneath indents (Fig. 8). At the very early stage of the indentation, i.e., at depths <200 nm, GNDs are generated and concentrate in the vicinity of the indenter

tip, while subgrains are not yet formed (stage I in Fig. 8). The depth range between 200 nm and 500 nm (stage II in Fig. 8) appears to be a transition regime [cf. Fig. 5(b) and (c)], while with increasing depth the GND volume expands, which can also be seen in Fig. 7. In stage III, subgrains were formed and clear subgrain boundaries as well as GNDs accumulating along certain directions appeared (cf. Fig. 6). Corroborating the existence of different hardness regimes, the bilinear ISE [8] appears to be an intrinsic property related to the dislocation mechanisms.

At the depth of ~ 500 nm, the dislocation density is high enough for low-angle grain boundaries to form and straight lines of increased GND density appear at the subgrains (Figs. 5 and 8), with an angle of ~ 70° between them. With the depth increasing to 2000 nm, the semi-circular GND concentrations assume a butterfly shape (Fig. 8), which indicates the activation of secondary dislocation sources close to the free sample surface. For the deep indents, the lines of increased dislocation density
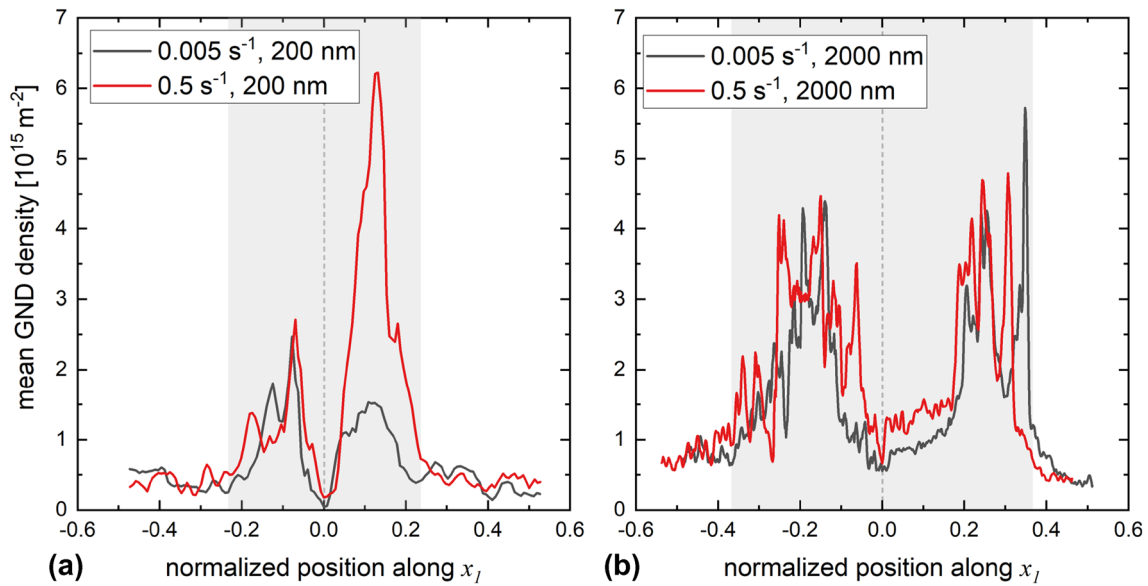
Figure 7: Comparison of the mean GND densities of the slow and fast indents, i.e., at strain rates of 0.005 s^{-1} and 0.5 s^{-1}, respectively, at indentation depths of (a) 200 nm and (b) 2000 nm. The x_1(RD) positions were normalized by the width of the scanned area and the center of the indent is located at x_1=0. The gray-shaded sections in (a) and (b) mark the center region of the indent to the depth of 200 nm and 2000 nm, respectively.
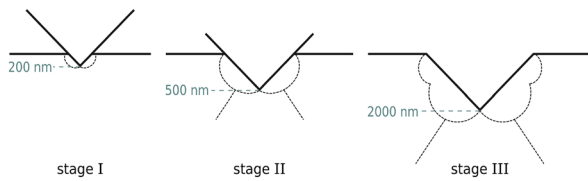

Figure 8: Schematic of the three different stages of the formation of the GND structure as observed on the cross sections of the wedge indents. From stage I to stage III, the indentation depth increases. The black dashed lines mark the regions with GND concentrations.

lying symmetrically at an angle of 35° to the center line (Fig. 5) can be understood in terms of rays of discontinuity as described by Rice [26]. Starting with the lattice rotations shown in Fig. 2, a general resemblance to the angular sectors near stationary crack tip fields [17, 27] can be seen.

Similar to a crack tip, the in-plane lattice rotation in Fig. 2 revealed angular sectors on both sides of the indent with discontinuously changing rotations of opposite signs in neighboring sectors. Shear and dislocations concentrate along the boundaries of such sectors and generate the rays of discontinuity [26]. According to Rice [26], for a stationary crack tip, the stress and deformation fields are supposed to be discontinuous and segmented into angular sectors, while the fields are continuous for a growing crack. The formation of sectors with positive and negative rotations underneath large wedge indents has indeed been observed experimentally for fcc metals [18–20]. The sectors were also reproduced by crystal plasticity [19, 30] and dislocation dynamics simulations [31]. In bcc metals, the concentrated shear was predicted as
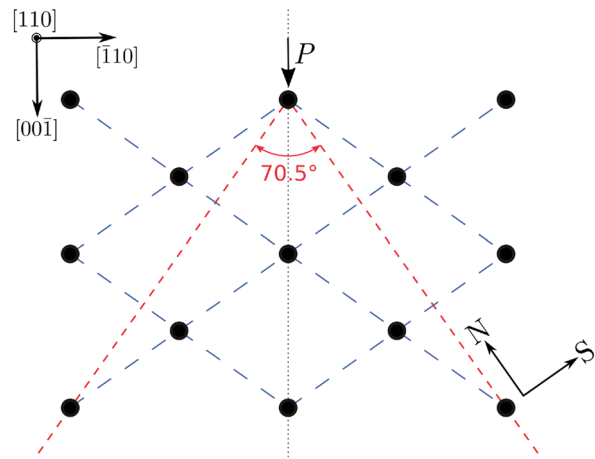

Figure 9: Schematic of the (110) plane in a bcc crystal. The atoms are denoted by the black circles. When a normal load P is applied along the [00$\bar{1}$] direction, the {110} slip plane families are activated with the traces highlighted by the blue dashed lines. N and S indicate the directions normal and parallel to one family of the {110} planes. The red lines represent the normal directions of the {110} planes with an angle of 70.5° in-between.

kink mode [26], which requires a series of dipole dislocations expanding across the activated slip planes. Thus, the rays of discontinuity in tungsten and bcc metals in general are supposed to be perpendicular to the traces of the slip planes. By contrast, for an fcc metal, the rays are usually parallel to the traces of the slip planes of the activated families (termed the regular mode) [26]. Figure 9 illustrates the (110) plane of a bcc crystal highlighting the positions of atoms and relevant

crystallographic directions. Since the cross sections of the wedge indents were (110) planes, the possible slip planes to be activated are the {110} families as also indicated in Fig. 4. The rays of discontinuity are shown as the red dashed lines with an angle of 70.5° corroborating our experimental findings (e.g., Figs. 2 and 4). Rays of discontinuity and angular sectors at a stationary crack tip of tungsten were described before [27], parallel to the {110} slip planes, though. However, on that (100) plane, the traces parallel and perpendicular to the {110} slip planes overlap both lying at an angle of 45° to the vertical axis. For the geometry in [27], it is therefore difficult to distinguish, whether the rays indicate regular or kink mode of the concentrated shear. The appearance of the rays at indentation depths > 500 nm marks the transition between two different deformation regimes and might be related to the change of constraints that are different in the proximity to the surface. Thus, also a variation of the wedge angle can be expected to affect the development of the GND structure with increasing indentation depth, while a detailed study of the transition regime or the constraint effect has not yet been conducted.

Summary and conclusions

Wedge indentation experiments were conducted on a (001) tungsten single crystal under the plane strain deformation condition. At different indentation depths and strain rates, the indentation-induced microstructures were characterized in detail using transmission Kikuchi diffraction and the dislocation density tensor. The plane strain deformation induced by wedge indentation offers a simplified, yet still quantitative, method to determine the dislocation structures. The microstructural features beneath the wedge indents revealed the correlation between the indentation strain field and the strain field at a stationary crack tip. The deformation condition is well controlled and such experiments can thus provide valuable input for computational studies of crack tips. Our main findings are as follows:

- The {110}⟨111⟩ slip system was experimentally confirmed as the primary activated edge dislocation system at room temperature under plane strain indentation. As expected, no screw dislocations were observed.
- At the different depths, the GND structures underneath wedge indents are distinctly different. At low depths, the GNDs are localized in the vicinity of the tip, while with increasing depth, the GND volume expands and subgrain boundaries form. The evolution of the GND structures with increasing depth corroborates the bilinear ISE as described recently [8].
- The GND density distributions depend on both the size of the indent and on the strain rate. The strain rate shows

a more pronounced influence on the GND density in the small depth regime than at the large depths. Presuming the hardness is affected by the GND density, the difference between hardness values is expected to be greater for shallow indents when comparing the data at different strain rates as indeed observed previously [8].

- At 2000 nm depth, the deformation fields underneath the wedge indents exhibit characteristics similar to the crack tip fields of a stationary crack [26], i.e., angular sectors and lines of higher GND density, which agree well with the shear sectors and rays of discontinuity described in [26].

Experimental methods

Sample preparation

Single-crystalline tungsten with (001) out-of-plane orientation was studied. The surface of the W crystal was gently polished mechanically using SiC paper and diamond suspensions of varying grain sizes. After polishing with 1 μm grain size diamond suspension, the final mechanical polishing step was with OP-A (acidic alumina) with 0.06 μm grain size. The electropolishing was conducted with a LectroPol electropolisher (Struers GmbH, Willich, Germany) at a voltage of 10 V for 30 s using 2 wt% NaOH solution. The surface roughness R_a was 0.009 μm, measured over an area of ~ 2.5 × 2.5 μm^2 using a laser scanning confocal microscope (VK-9710K, Keyence Corporation, Osaka, Japan). The out-of-plane orientation of the W single crystal was confirmed as (001) by electron backscatter diffraction.

Indentation experiments

A wedge-shaped diamond indenter tip with a tip angle of 90° and a wedge length of 25 μm was used to indent the (001) tungsten single crystal (tip radius <10 nm, evaluated by TEM of cross section through an indent.). The wedge was aligned with the [110] direction on the (001) crystallographic plane. The indentation experiments were performed using a Nano Indenter G200 XP (Agilent/Keysight Technologies, Inc., CA, USA). Quasi-static indentation experiments at constant strain rates were conducted. Three different indentation strain rates $\frac{\dot{P}}{P}$ (with P as the indentation load) were applied, i.e., 0.005 s^{-1}, 0.05 s^{-1}, and 0.5 s^{-1}. Indents to depths of 150 nm and 200 nm (referred to as the small depth regime in the following) and to 500 nm and 2000 nm (termed the large depth regime) were performed at each strain rate. The indentation depths were selected to cover the behaviors in two distinctly different depth regimes [8] and to maintain a comparable interval in terms of 1/h between indentation depths in the two regimes.

Transmission Kikuchi diffraction measurements

TKD measurements were conducted on thin lamellae prepared from cross sections perpendicular to the wedge imprints at mid-length [Fig. 10(a)]. The TKD lamellae were prepared using the focused ion beam (FIB) of a Helios NanoLab 650 DualBeam microscope (FEI Company, now Thermo Fischer Scientific, Inc., MA, U.S.A) applying a standard lift-out process. First, Pt was deposited on the surface of the indents to protect the region of interest during the FIB milling. Large trenches on both sides of the region of interest were milled with the Gallium ion beam at 30 kV acceleration voltage, while the beam current was reduced from 45 to 0.77 nA until a lamella thickness of approximately

~1 µm was achieved. The lamella was then transferred to a Cu grid, and the final thickness of ~100 to 150 nm was achieved by further thinning and polishing using the Gallium ion beam at reduced beam currents and acceleration voltages. The overall process is summarized in Fig. 10.

The TKD measurements were carried out with two different systems, i.e., the AZtec EBSD system with AZtecHKL software (Oxford Instruments GmbH, Wiesbaden, Germany) and the high-definition EBSD detector e⁻ Flash^{HD} (QUANTAX EBSD, Bruker Nano GmbH, Berlin, Germany). The comparison of data from the two different setups shown in the Supplementary materials reveals no significant variations of
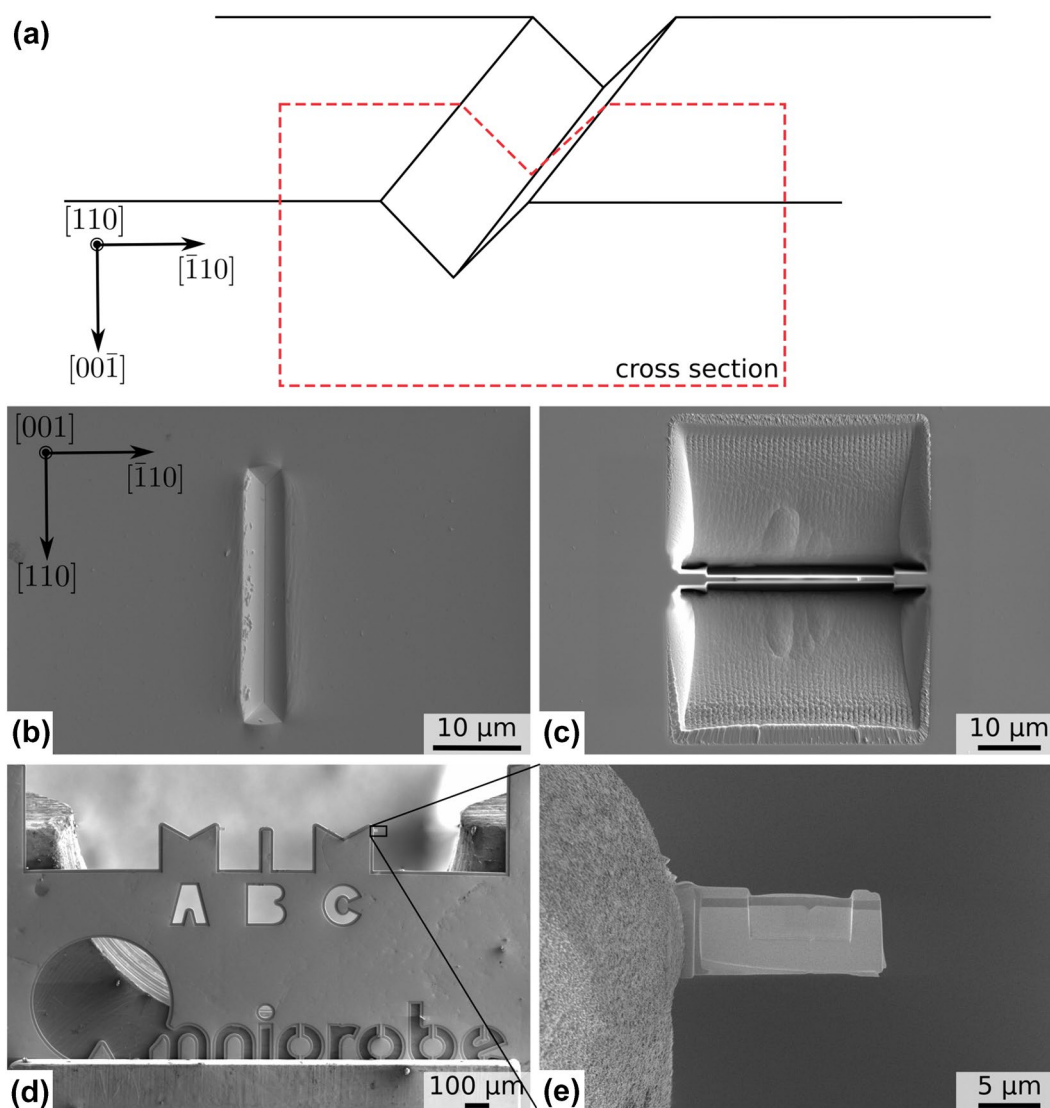

Figure 10: Electron-transparent lamellae of cross sections underneath wedge indents were prepared for the TKD analysis using a FIB. (a) The wedge was aligned with specific crystallographic directions to achieve a plane strain condition. The lamella was then prepared via a lift-out process from the mid-section of the indent. (b)–(e) show the main FIB preparation steps. After the indentation and Pt deposition, a thin section (~ 1 µm thickness) was prepared by FIB milling. The lamella was then transferred to a Cu grid. The region of interest beneath the indent was then further thinned to the final thickness of ~ 100 to 150 nm.

the experimental results. The acceleration voltage and beam current of the electron beam were the same for all measurements, i.e., 30 kV and 6.4 nA, respectively. The step size was kept between 7 and 12 nm for shallow indents and to 12–20 nm for bigger indents. To reduce the influence of varying step size on the GND density determination, the step size was kept in a comparable range, while it was adjusted with respect to the size of the deformed region, the detector capacity and, thus, the measurement time. The TKD data were analyzed using an in-house developed MATLAB program based on the MTEX Toolbox [32–34].

The 2D TKD data contain information about the position of the individual points (x_1, x_2) in a Cartesian coordinate system and the crystallographic orientation described by the three Euler angles $(\varphi_1, \Phi, \varphi_2)$, according to the Bunge convention [35]. The Bunge Euler angles describe the relative angles between the tungsten crystallographic system and the reference system, i.e., the sample system. After three rotations determined by the three Euler angles, the crystallographic system will coincide with the sample system. Under the plane strain condition, the deformation occurs in-plane only and, thus, both Φ and φ_2 are constant.

Acknowledgments

Funding

Data availability

Data will be made available upon reasonable request.

Declarations

Conflict of interest The authors declare that they have no competing financial interests or personal relationships that could have appeared to influence the work reported in this paper.

Open Access

Supplementary Information

The online version contains supplementary material available at https://doi.org/10.1557/s43578-022-00733-9.

References

1. J.R. Stephens, Review of deformation behavior of tungsten at temperature less than 0.2 absolute melting temperature, NASA Technical Memorandum TM X-2482 (1972)

2. E. Lassner, W.-D. Schubert, *Tungsten: Properties, Chemistry, Technology of the Element, Alloys, and Chemical Compounds* (Springer, Boston, 1999)

3. J.R. Greer, J.T.M. De Hosson, Plasticity in small-sized metallic systems: intrinsic versus extrinsic size effect. Prog. Mater. Sci. **56**(6), 654–724 (2011). https://doi.org/10.1016/j.pmatsci.2011.01.005

4. G.M. Pharr, E.G. Herbert, Y. Gao, The indentation size effect: a critical examination of experimental observations and mechanistic interpretations. Annu. Rev. Mater. Res. **40**(1), 271–292 (2010). https://doi.org/10.1146/annurev-matsci-070909-104456

5. K. Durst, B. Backes, O. Franke, M. Göken, Indentation size effect in metallic materials: modeling strength from pop-in to macroscopic hardness using geometrically necessary dislocations. Acta Mater. **54**(9), 2547–2555 (2006). https://doi.org/10.1016/j.actamat.2006.01.036

6. V. Maier, C. Schunk, M. Göken, K. Durst, Microstructure-dependent deformation behaviour of bcc-metals—indentation size effect and strain rate sensitivity. Phil. Mag. **95**(16–18), 1766–1779 (2015). https://doi.org/10.1080/14786435.2014.982741

7. F. Javaid, Y. Xu, E. Bruder, K. Durst, Indentation size effect in tungsten: Quantification of geometrically necessary dislocations underneath the indentations using hr-ebsd. Mater. Charact. **142**, 39–42 (2018). https://doi.org/10.1016/j.matchar.2018.05.016

8. J. Wang, T. Volz, S. Weygand, R. Schwaiger, The indentation size effect of single-crystalline tungsten revisited. J. Mater. Res. (2021). https://doi.org/10.1557/s43578-021-00221-6

9. W.D. Nix, H. Gao, Indentation size effects in crystalline materials: a law for strain gradient plasticity. J. Mech. Phys. Solids **46**(3), 411–425 (1998). https://doi.org/10.1016/S0022-5096(97)00086-0

10. D. Kiener, R. Pippan, C. Motz, H. Kreuzer, Microstructural evolution of the deformed volume beneath microindents in tungsten and copper. Acta Mater. **54**(10), 2801–2811 (2006). https://doi.org/10.1016/j.actamat.2006.02.024

11. L.N. Brewer, D.P. Field, C.C. Merriman, Mapping and assessing plastic deformation using EBSD. Electron Backscatter Diffraction Mater. Sci. **18**, 251–262 (2009)

12. J. Nye, Some geometrical relations in dislocated crystals. Acta Metall. **1**(2), 153–162 (1953). https://doi.org/10.1016/0001-6160(53)90054-6

13. E. Kröner, Allgemeine Kontinuumstheorie der Versetzungen und Eigenspannungen. Arch. Ration. Mech. Anal. **4**(1), 273 (1959). https://doi.org/10.1007/BF00281393

14. E. Demir, D. Raabe, N. Zaafarani, S. Zaefferer, Investigation of the indentation size effect through the measurement of the geometrically necessary dislocations beneath small indents of different depths using ebsd tomography. Acta Mater. **57**, 559–569 (2009). https://doi.org/10.1016/j.actamat.2008.09.039

15. P. Konijnenberg, S. Zaefferer, D. Raabe, Assessment of geometrically necessary dislocation levels derived by 3D EBSD. Acta Mater. **99**, 402–414 (2015). https://doi.org/10.1016/j.actamat.2015.06.051

16. S. Kalácska, J. Ast, P.D. Ispánovity, J. Michler, X. Maeder, 3D HR-EBSD characterization of the plastic zone around crack tips in tungsten single crystals at the micron scale. Acta Mater. **200**, 211–222 (2020). https://doi.org/10.1016/j.actamat.2020.09.009

17. J.W. Kysar, C.L. Briant, Crack tip deformation fields in ductile single crystals. Acta Mater. **50**(9), 2367–2380 (2002). https://doi.org/10.1016/S1359-6454(02)00070-8

18. J.W. Kysar, Y.X. Gan, T.L. Morse, X. Chen, M.E. Jones, High strain gradient plasticity associated with wedge indentation into face-centered cubic single crystals: geometrically necessary dislocation densities. J. Mech. Phys. Solids **55**, 1554–1573 (2007). https://doi.org/10.1016/j.jmps.2006.09.009

19. J. Kysar, Y. Saito, M. Oztop, D. Lee, W. Huh, Experimental lower bounds on geometrically necessary dislocation density. Int. J. Plast **26**(8), 1097–1123 (2010). https://doi.org/10.1016/j.ijplas.2010.03.009

20. C. Dahlberg, Y. Saito, M. Öztop, J. Kysar, Geometrically necessary dislocation density measurements associated with different angles of indentations. Int. J. Plast **54**, 81–95 (2014). https://doi.org/10.1016/j.ijplas.2013.08.008

21. S. Zaefferer, A critical review of orientation microscopy in SEM and TEM. Cryst. Res. Technol. **46**(6), 607–628 (2011). https://doi.org/10.1002/crat.201100125

22. T. Tokarski, G. Cios, A. Kula, P. Bała, High quality transmission kikuchi diffraction analysis of deformed alloys—case study. Mater. Charact. **121**, 231–236 (2016). https://doi.org/10.1016/j.matchar.2016.10.013

23. G.C. Sneddon, P.W. Trimby, J.M. Cairney, Transmission Kikuchi diffraction in a scanning electron microscope: a review. Mater. Sci. Eng. R. Rep. **110**, 1–12 (2016). https://doi.org/10.1016/j.mser.2016.10.001

24. A.A. Gazder, K.I. Elkhodary, M.J. Nancarrow, A.A. Saleh, Transmission Kikuchi diffraction versus electron back-scattering diffraction: a case study on an electron transparent cross-section of TWIP steel. Micron **103**, 53–63 (2017). https://doi.org/10.1016/j.micron.2017.09.008

25. W. Pantleon, Resolving the geometrically necessary dislocation content by conventional electron backscattering diffraction. Scripta Mater. **58**(11), 994–997 (2008). https://doi.org/10.1016/j.scriptamat.2008.01.050

26. J.R. Rice, Tensile crack tip fields in elastic-ideally plastic crystals. Mech. Mater. **6**(4), 317–335 (1987). https://doi.org/10.1016/0167-6636(87)90030-5

27. E. Tarleton, S. Roberts, Dislocation dynamic modelling of the brittle-ductile transition in tungsten. Philos. Mag. **89**(31), 2759–2769 (2009). https://doi.org/10.1080/14786430902992619

28. G.I. Taylor, The mechanism of plastic deformation of crystals. Part. I. Theoret. Proc. R. Soc. Lond. Ser. A **145**(855), 362–387 (1934). https://doi.org/10.1098/rspa.1934.0106

29. K. Durst, B. Backes, M. Göken, Indentation size effect in metallic materials: correcting for the size of the plastic zone. Scripta Mater. **52**(11), 1093–1097 (2005). https://doi.org/10.1016/j.scriptamat.2005.02.009

30. Y. Saito, M.S. Oztop, J.W. Kysar, Wedge indentation into elastic-plastic single crystals. 2: simulations for face-centered cubic crystals. Int. J. Plast. **28**(1), 70–87 (2012). https://doi.org/10.1016/j.ijplas.2011.05.013

31. Y. Zhang, Y. Gao, L. Nicola, Lattice rotation caused by wedge indentation of a single crystal: dislocation dynamics compared to crystal plasticity simulations. J. Mech. Phys. Solids **68**, 267–279 (2014). https://doi.org/10.1016/j.jmps.2014.04.006

32. MTEX Toolbox, [Online]. https://mtex-toolbox.github.io/

33. T. Skippon. https://github.com/tskippon/GND

34. A. Arsenlis, D. Parks, Crystallographic aspects of geometrically-necessary and statistically-stored dislocation density. Acta Mater. **47**(5), 1597–1611 (1999). https://doi.org/10.1016/S1359-6454(99)00020-8

35. H.-J. Bunge, The orientation distribution function of the crystallites in cold-rolled and annealed low-carbon steel sheets. Physica Status Solidi (B) **26**(1), 167–172 (1968). https://doi.org/10.1002/pssb.19680260116